V.B. NEIMASH,[1] A.O. GOUSHCHA,[1, 2] P.E. SHEPELIAVYI,[3] V.O. YUKHYMCHUK,[3] V.A. DAN'KO,[3] V.V. MELNYK,[4] A.G. KUZMICH [4]

[1] Institute of Physics, Nat. Acad. of Sci. of Ukraine
  (46, Nauky Ave., Kyiv 03680, Ukraine; e-mail: neimash@gmail.com)

[2] NuPortSoft
  (21 Nopalitos Way, Aliso Viejo, CA 92656, USA)

[3] V.E. Lashkaryov Institute of Semiconductor Physics, Nat. Acad. of Sci. of Ukraine
  (45, Nauky Ave., Kyiv 03028, Ukraine)

[4] Taras Shevchenko National University of Kyiv, Faculty of Physics
  (64/13, Volodymyrs'ka Str., Kyiv 01601, Ukraine)

MECHANISM OF TIN-INDUCED CRYSTALLIZATION IN AMORPHOUS SILICON

Formation of Si nanocrystals in amorphous Si-metallic Sn film structures has been studied experimentally, by using the Auger spectroscopy, electron microscopy, and Raman scattering methods. The results are analyzed in comparison with recent results on the crystallization of tin-doped amorphous Si. A mechanism of silicon transformation from the amorphous to the nanocrystalline state in the eutectic layer at the Si–Sn interface is proposed. The mechanism essence consists in a cyclic repetition of the processes of formation and decay of the Si–Sn solution. The application aspect of this mechanism for the fabrication of nanosilicon films used in solar cells is discussed.

K e y w o r d s: silicon, nanocrystals, thin films, metal-induced crystallization, tin, solar cell.

1. Introduction

Researches of silicon transformation processes from the amorphous into the crystalline state are challenging owing to the requirements put forward by the development of technologies aimed at fabricating the materials for photo-electric converters of solar energy, in particular, thin films of nanocrystalline silicon (nc-Si) [1]. At crystal sizes of a few nanometers, silicon reveals a number of physical properties that are important for the manufacture of solar cells. Namely, these are the direct-band-gap mechanism of optical absorption, the diffusion length of nonequilibrium charge carriers sufficient for their effective collection, the absence of the Staebler–Wronski effect [2], and the ability to change the energy gap width depending on the nanocrystal size. The difficulty consists in the absence of a technology that would allow one to control the dimensions of Si nanocrystals rather easily. One of the ways to solve it is the search for methods to controllably transform silicon from the amorphous (a-Si) into the nanocrystalline state with the use of the metal-induced crystallization [3–6].

Tin (Sn) occupies a special place among metals suitable for the metal-induced crystallization. Tin does not create energy levels in the energy gap of Si. Therefore, the doping with tin within the solubility limits does not affect the final electric, optical, and recombination characteristics of Si crystals. At the same time, the presence of Sn atoms in Si substantially slows down the degradation of those characteristics under the action of defect-forming factors, in particular, at thermal treatments (TTs) [7–9] and under ionizing irradiation [9–12].

The influence of the Sn impurity on properties of amorphous Si is stronger. For example, the doping with tin considerably reduces the optical width of the Si energy gap E_g [13, 15]. As the Sn concentration increases, the mechanism of electroconductivity changes from the activation to the hopping one [15, 16], and light can be absorbed following both the direct- and indirect-band-gap mechanisms [16,17]. Tin atoms in a-Si can be at the substitution sites in both the tetragonal [18] and non-tetragonal [17] configurations to form a regular or non-regular mesh. Under certain conditions, precipitates of Sn atoms can be formed in the amorphous Si matrix [16, 19].

Tin forms an eutectic alloy with silicon [20]. In addition, it can induce a transition of Si from the
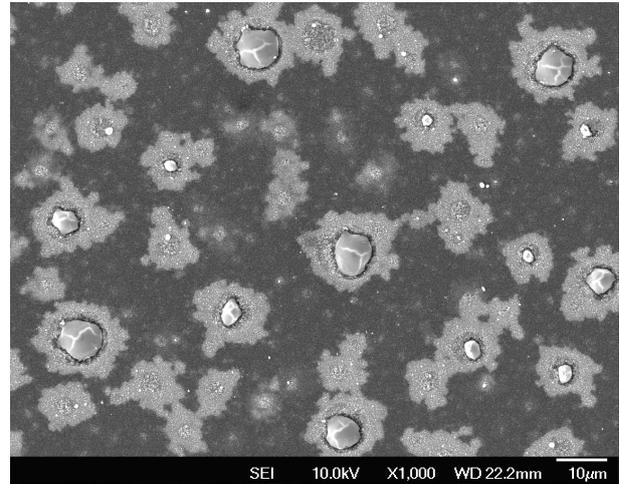
amorphous state into the crystalline one owing to the exchange layer effect at the metal-silicon interface [3, 21]. Such metal-induced crystallization was observed at the annealing of sandwich structures composed of amorphous Si and metallic Sn films deposited onto glass substrates [3, 22]. A considerable acceleration of the a-Si crystallization was observed at the growth of thin films of $Si_{1-x}Sn_x$ alloys deposited from the vapor phase [23]. However, this effect may also be induced by the surface in the case of the non-uniform distribution of Sn atoms across the film thickness [24]. Taking this fact into account, the influence of various tin concentrations on the microstructure of Si:Sn film alloys was analyzed in work [25], where its threshold character was revealed. At tin concentrations below about 1.5–2.0 at.%, the alloy is only amorphous. At higher Sn concentrations in the alloys, there appear Sn crystals 2–4 nm in dimensions, with their volume fraction being proportional to the tin concentration.

If the tin concentration in a Si–Sn alloy exceeds this threshold, inclusions of metallic tin emerge [25]. This fact may mean that the limit of the Sn solubility in amorphous Si is exceeded. Then it can explain the transition of the electroconductivity mechanism from the activation to the hopping type, which was known earlier to occur just at the indicated concentrations of tin in silicon [15, 16]. The coincidence of the threshold values for the influence of tin concentration in those three processes at the quantitative level, the emergence of metallic Sn droplets, and the change of an electroconductivity type may testify that it is the droplets of metallic tin that initiate the crystallization in tin-doped amorphous Si. This hypothesis agrees well with the data concerning the crystallization of a-Si at thermal treatments of planar sandwich structures Si-Sn [3, 22].

Developing the idea concerning the role of the eutectic exchange layer arising at the interface metal–amorphous silicon, which was put forward in work [21], we proposed a hypothesis about the mechanism of tin-induced Si transformation from the amorphous into the crystalline state by means of the cyclic formation-decay process of a Si solution in microscopic liquid Sn droplets in the volume of amorphous silicon [25].

This work aimed at the experimental verification of the hypothesis mentioned above. The idea of verification consisted in simulating the proposed mechanism
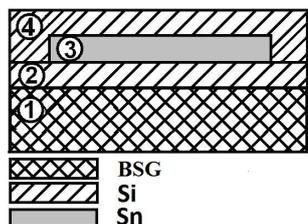

Fig. 1. SEM image of the surface of a Si:Sn alloy film. The Sn content is 5 at.%. The film thickness is 500 nm
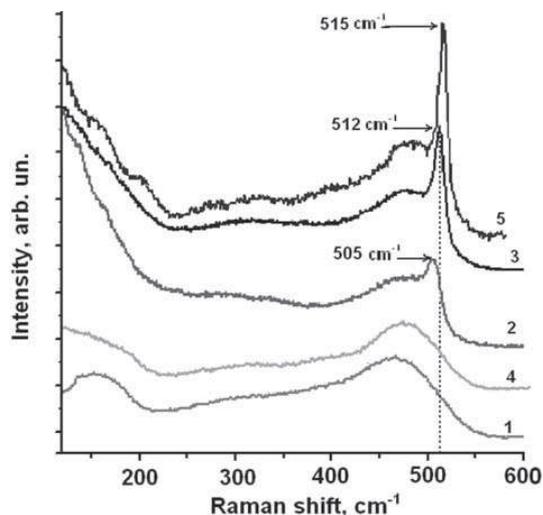
by forming a macroscopic tin droplet in the bulk of an amorphous silicon film and studying its influence on the structure of surrounding Si in the course of thermal treatments (TTs).

2. Experiment

In Fig. 1, a scanning electron microscopy (SEM) image of the surface of a film of the Si–Sn alloy deposited by thermally evaporating a mixture of Si and Sn vapors in vacuum on a glass substrate at a temperature of 300 °C, in accordance with the technology described in work [25], is exhibited. As was shown in work [25], the quasi-spherical inclusions surrounded by dendrite-like auras are droplets of metallic Sn. At the same time, the auras in the SEM image (Fig. 1) are regions of Si crystallization, whereas the dark sections correspond to amorphous Si. Since the size of some Sn droplets exceeds the nominal film thickness, the Si–Sn interface is clearly distinguished for them. For large Sn droplets, one can monitor the distribution of nanocrystalline cluster dimensions over the distance to the interface [25]. Smaller auras without Sn droplets at the center may contain them in the film bulk, or they can be dissolved at all. It is difficult to monitor the Sn concentration distribution across such films and its evolution at the TT, which is necessary to check the indicated hypothesis. Therefore, we used a model analog of a planar Sn droplet in the a-Si environment, which is convenient for Auger re-

Fig. 2. Schematic diagram of the planar structure for simulating the mechanism of amorphous Si-Sn alloy crystallization: (*1*) borosilicate glass substrate, (*2*) lower a-Si layer, (*3*) Sn metal, (*4*) upper a-Si layer

Fig. 3. Raman spectra of BSG/Si/Si (*1* and *4*) and BSG/Si/Sn/Si (*2, 3,* and *5*) structures: before (*1* and *2*) and after TT at 300 (*3* and *4*) or 400 °C (*5*) for 30 min

searches. This is an Sn film, which is macroscopic in the lateral directions (a scale of about 1 cm) and microscopic in the transverse direction (a thickness of about 100 nm), surrounded by amorphous Si.

The model tin droplet has a planar structure schematically depicted in Fig. 2. It was fabricated by thermally evaporating Si (a single crystal of electronic purity) and, separately, Sn (a purity of 99.92%) in vacuum.

The structure formation occurred in three stages. On the first stage, a layer of amorphous silicon 100 nm in thickness (2) was deposited on a borosilicate glass (BSG) substrate 76×76 mm^2 in dimensions at a temperature of about 150 °C. At the second stage, a layer of metallic tin (3) also 100 nm in thickness and 60×60 mm^2 in area was deposited onto layer 2 using

a corresponding mask. At the third step, the second layer of amorphous Si (4) also 100 nm in thickness and 76×76 mm^2 in area was formed above layers 2 and 3. All three stages were carried out in a vacuum chamber at a residual pressure of 10^{-3} Pa by sequentially using three different evaporators. No additional TT was applied. As a result, a fragment of the metallic tin film surrounded from all sides by a film of amorphous silicon was fabricated. To a certain extent, this structure can be considered as an analog of the model of tin micro-droplet in amorphous Si, which was proposed in work [25] and used to explain the mechanism of tin-induced crystallization in amorphous silicon.

The ratio between the amorphous and crystalline phase components of Si, as well as the dominating size of Si crystallites in the amorphous matrix, was determined by analyzing the Raman spectra excited by a Jobin Yvon T-64000 argon laser with a wavelength of 514.5 nm and registered at room temperature. The diameter of a light exciting spot was varied from 3 to 300 μm. The concentration distribution profiles of chemical elements across the film thickness were studied using the Auger spectroscopy method at ionic etching (Riber Las 2000). The scanning electronic microscopy (SEM) was applied to study the surface topology of the structure (JSM-840).

3. Results and their Discussion

Figure 3 demonstrates the Raman spectra measured at various sites of the examined BSG/Si/Sn/Si structure: as-fabricated (*1* and *2*) and after its thermal treatment in vacuum for 30 min at 300 (*3* and *4*) and 400 °C (*5*). Spectra *1* and *4* were registered on the peripheral part of the surface, where the tin layer is absent; and spectra *2, 3,* and *5* on the central part of the structure above the tin layer.

One can see that spectra *1* and *4* with a wide band peaked at about 470 cm^{-1} almost coincide. They correspond to a purely amorphous Si state. This means that, in the absence of Sn in the Raman measurement zone, the phase state of a-Si does not change after the thermal treatment at temperatures up to 300 °C inclusive. On the contrary, spectra *2, 3,* and *5*, which were measured above the tin layer in the same specimen, contain an additional sharp peak at 505, 512, and 515 cm^{-1}, respectively, which corresponds to the crystalline Si phase. In other words, the material structure in this section of the specimen is an amorphous-crystalline composite.

The resolution of Raman spectra into two components, as is shown in Fig. 4, and the application of the algorithm presented in work [25] allowed us to estimate the dominant sizes of silicon crystals according to the model of spatial phonon correlation [26,27] and the volume ratios between the crystalline and amorphous phases in the composite.

From Fig. 3 (spectrum *2*), one can see that metallic Sn induces the crystallization in amorphous Si already in the course of BSG/Si/Sn/Si structure fabrication. The analysis of Raman spectra showed that the dominant size of crystals increased from 2.7 nm in the as-fabricated specimen to 3.2 nm after the TT of the specimen at 300 °C and to 4.5 nm after its TT at 400 °C. Correspondingly, the content of the nanocrystalline Si phase (nc-Si) grew more than two times. Those results correspond to the data obtained in works [3, 22, 25].

In Fig. 5, the concentration distributions of chemical elements across the Si/Sn/Si structure thickness are plotted. They were obtained by measuring the Auger spectra, while sputtering the layers using Ar^+ ions with an energy of 3 keV. The sputtering rate amounted to 12–14 nm/min. The left edges of the distributions shown in Fig. 5 correspond to the external surface of the central section of the structure exhibited in Fig. 2. The right edges correspond to the BSG substrate.

High contents of oxygen and carbon technological impurities in the formed films resulted from a low level of vacuum in the course of impurity deposition and a subsequent atmospheric oxidation of the surface. In Fig. 5, one can clearly distinguish two concentration maxima of Si with an Sn maximum between them, which correspond to three layers deposited on the substrate. At the same time, the attention is attracted to an unusual concentration ratio between tin and silicon in each of three layers of the structure. First, the maximum concentration of silicon in the external layer (about 60 at.%) is 1.5 times lower than the maximum Si concentration in the internal layer (about 90 at.%). Second, the maximum tin concentration does not exceed 45 at.%, being almost equal to the Si concentration. At first sight, this looks strange, because the layers in the Si-Sn-Si structure were formed sequentially and under conditions that would provide an identical thickness of about 100 nm for every layer, should it be deposited onto the glass substrate alone.
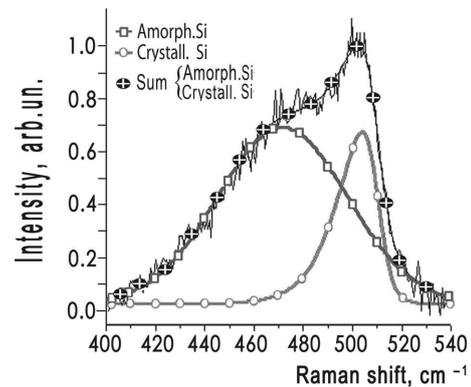

Fig. 4. Resolution of Raman spectra, as described in work [25], into the Gaussian corresponding to the amorphous phase (the green line with squares) and the asymmetric component corresponding to the crystalline phase (the red line with circles) for the BSG/Si/Sn/Si structure before TT. The black curve with circles and white crosses is a sum of components
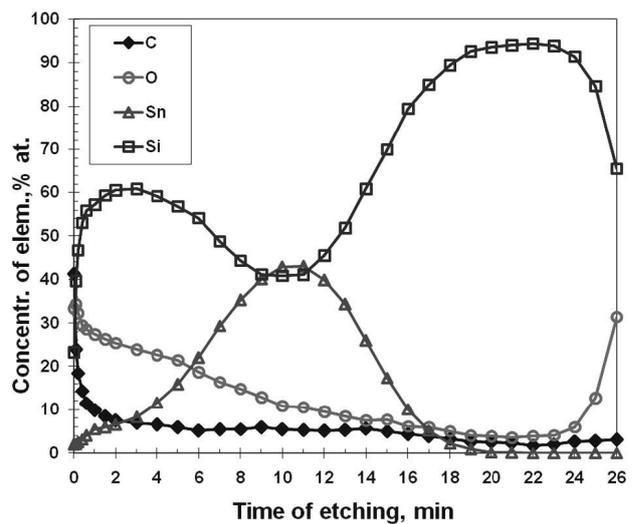

Fig. 5. Concentration profiles of elements across the BSG/Si/Sn/Si structure thickness before a thermal treatment

Those results can be explained with regard for the results of electron microscopy researches of the Si/Sn/Si structure carried out in the secondary electron mode. They are shown in Fig. 6. It is evident that the surface of the as-fabricated Si–Sn–Si structure consists of microscopic balls from 120 to 470 nm in diameter. The majority of balls have diameters of about 300 nm. The reflection of visible light from this surface is very low, and the latter looks black. The balls are covered with a characteristic crack-like orna-
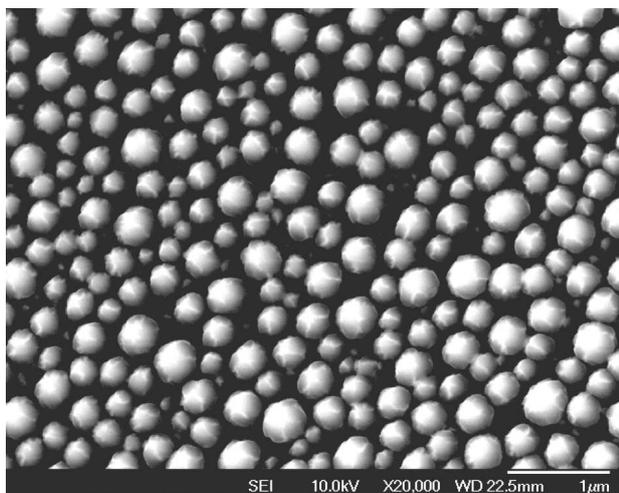
Fig. 6. SEM images of the BSG/Si/Sn/Si structure surface before a thermal treatment
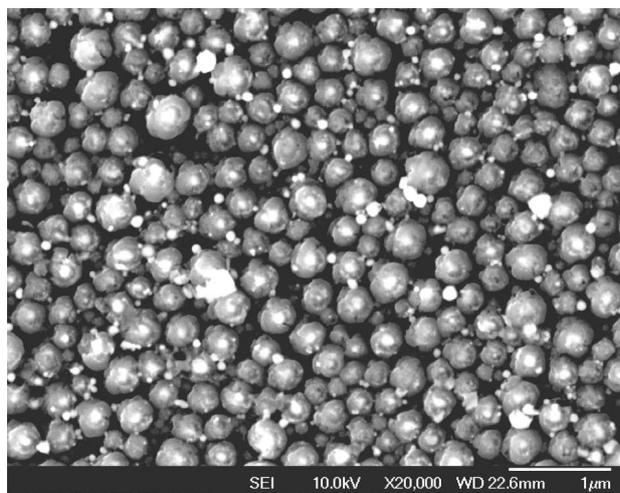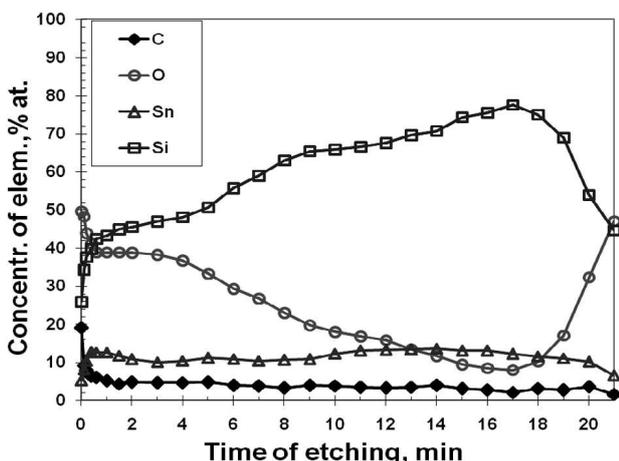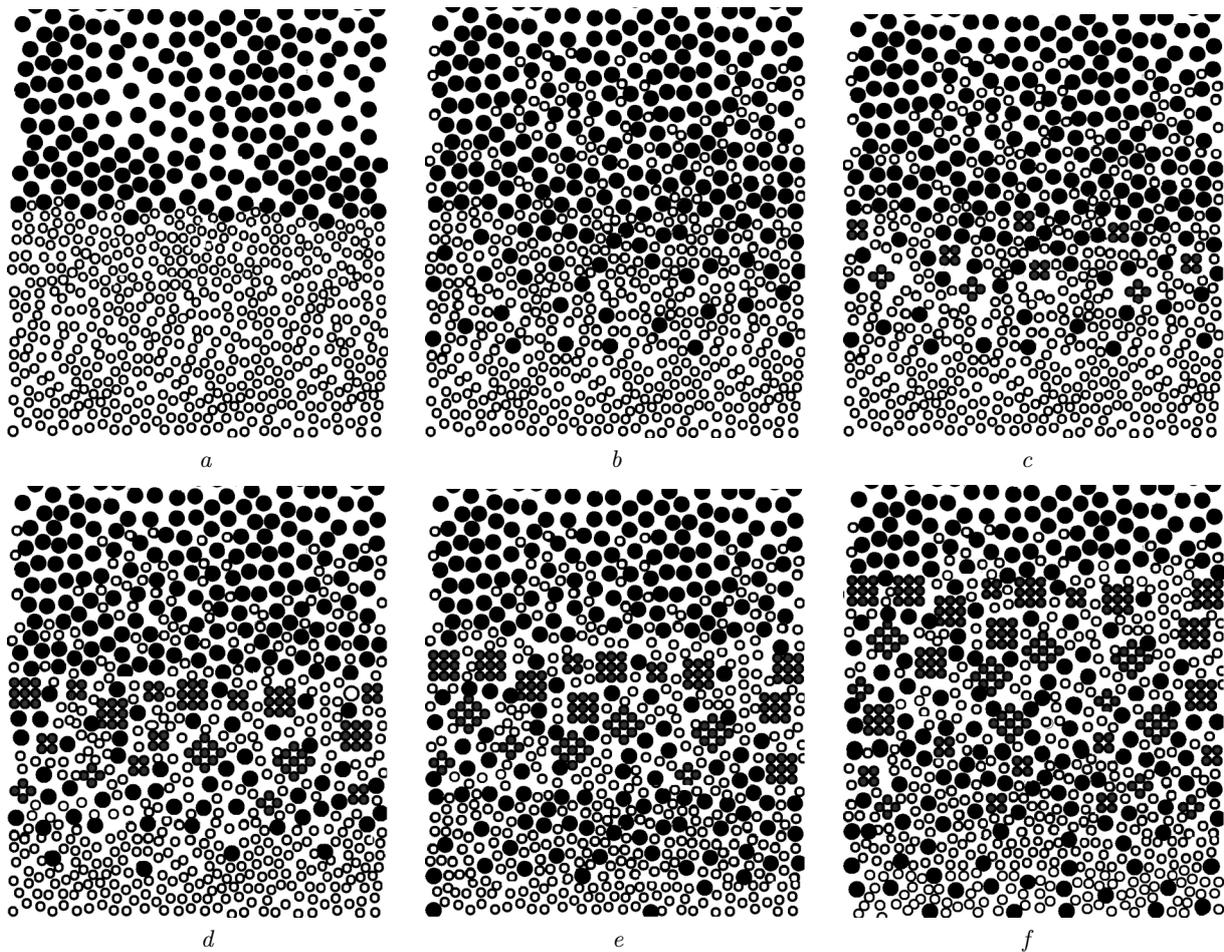

Fig. 7. The same as in Fig. 5, but after TT at 300 °C

ment similar to that on tin balls in the Si:Sn film alloy (Fig. 1). Those cracks might probably arise at cooling owing to the difference between the coefficients of thermal expansion of tin in the ball core (the light areas of the ornament) and silicon in the ball shell (the grey areas).

Of course, Fig. 5 exhibits the distributions of elements averaged over the thickness of the layer composed of tin balls covered with a silicon shell (Fig. 6). Every ball consists of a tin core covered with a silicon shell. Therefore, the integral Auger analysis registers a smeared maximum of the tin concentration at the depth equal to the average ball radius. This structure

Fig. 8. The same as in Fig. 6, but after TT at 300 °C

was probably formed when depositing the second Si layer on the droplets of liquid Sn. The Sn droplets may be formed as a result of the surface tension forces [3, 6] when the tin film was fused by the atomic and radiation flows from the silicon evaporator.

Figure 7 demonstrates the element distributions across the Si/Sn/Si structure thickness after its 30-min annealing at 300 °C. In comparison with Fig. 5, it is evident that the distributions of C and O technological impurities were not changed substantially. Only the oxygen content increased a little. This fact can be related to the additional oxidation of the specimen surface when the specimens were in the air atmosphere. Attention is attracted by the disappearance of the tin concentration maximum and the silicon concentration minimum in the etching time interval of 10–12 min observed in Fig. 5. Tin became uniformly distributed across the whole structure thickness from the surface to the substrate. Silicon also became distributed more uniformly in comparison with Fig. 5. The Raman spectra show that the corresponding content of the crystalline Si phase increased by approximately a factor of two. In other words, during the TT at 300 °C, silicon is mixed with tin and partially transformed from the amorphous into the crystalline state. Figure 8 illustrates how the surface of the BSG/Si/Sn/Si structure changed after this process. One can see that, instead of a crack-like ornament, there emerged light bumps on the balls and smaller white balls between initial grey balls. The contrast of the SEM image characterizes the electron

Fig. 9. Schematic illustration of the time-dependent changes at the interface between amorphous silicon and liquid tin, which explains the process of a-Si transformation into nc-Si through its dissolution in tin

concentration at the reflecting surface. Therefore, it is possible to suppose that white spots on the image correspond to metallic tin.

4. Discussion

Hence, our model macrodroplet prepared in the form of a tin film embedded in a Si–Sn–Si sandwich structure has fused and decayed into microdroplets as early as in the course of the second Si layer deposition. This layer was accumulated on microdroplets of liquid Sn. It formed a shell of balls shown in Fig. 6 and the corresponding distribution of chemical elements across the thickness (Fig. 5). Within the time interval when tin remained liquid in the balls, Si might probably crystallize partially, which is evidenced by curve *2*

in Fig. 3. The silicon crystallization continued during the additional TT, when the tin cores of balls became liquid again (curves *3* and *5* in Fig. 3). The Auger researches testify that, at this stage, tin becomes uniformly redistributed across the whole thickness of the structure (Fig. 7).

Let us consider, in detail, a physical model that explains the process of partial crystallization of amorphous silicon with the participation of liquid metallic Sn proposed by us in work [25]. In Fig. 9, *a*, light circles stand for the atoms of amorphous silicon, and dark ones for the atoms of liquid tin. Owing to the screening of Si bonds by free electrons in the metal [28] and to the diffusion, the silicon and tin atoms "cross" the Si/Sn interface and partially mix together (Fig. 9, *b*). As a result, the layer of an eutectic silicon
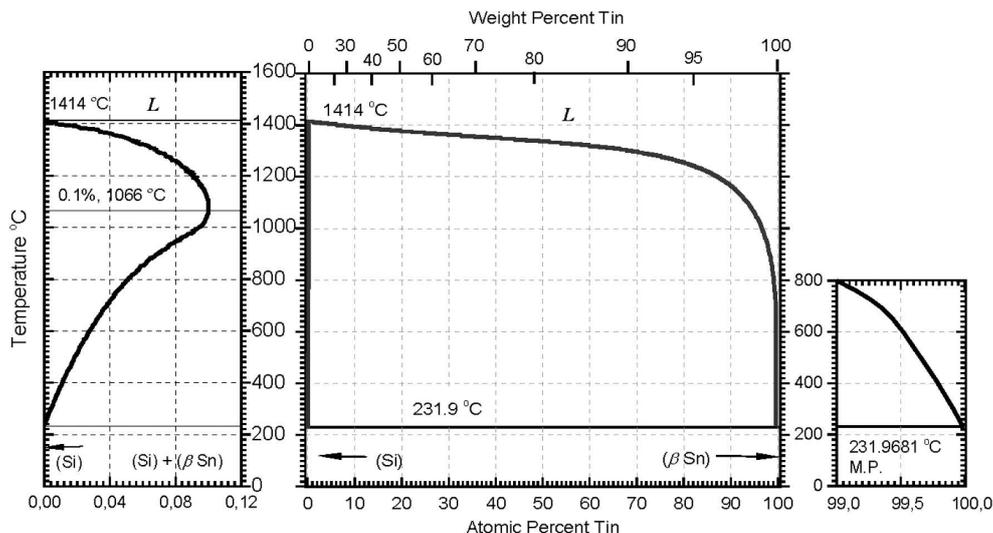
Fig. 10. Phase diagram for the system Si–Sn according to the data of work [20]

solution in tin is formed. The dissolution of amorphous silicon is known to occur, being accompanied by the heat absorption. Therefore, as the solution enrichment with silicon continues, the solution temperature decreases, and, at a certain stage, the solution becomes oversaturated. As a result, the dissolved silicon atoms precipitate, i.e. they agglomerate into groups with the crystalline structure (ordered groups of grey or red circles in Fig. 9, *c*). The number of such groups increases, and they become bigger (Figs. 9, *d–f*). In real structures, their analog is nanocrystals, which were registered in Raman spectra (Fig. 3, spectra *2, 3,* and *5*).

The silicon crystallization in liquid tin initiates two processes, which bring the system into the previous state. One of them is the tin segregation on the surface of growing silicon crystals. The threshold solubility of tin in crystalline silicon is known to be low (about 5×10^{19} cm^{-3} [20, 29, 30]). Therefore, the dissolved silicon atoms, which group into clusters in the form of nanocrystals, squeeze out tin atoms back to the eutectics, making the solution unsaturated. The other process is the release of a crystallization heat during the nanocrystal formation. It elevates the temperature and also reduces the saturation of a silicon solution in tin, so that the process of dissolution of amorphous silicon is resumed. Those two processes cyclically repeat, by resulting in the growth of new nanocrystals and the expansion of the crystallization zone in amorphous silicon around the Sn droplet. The

accumulation of nanocrystals during the dissolution of amorphous silicon is provided by the fact that their solubility in tin is much lower than the solubility of amorphous silicon. Really, the absence of a crystal symmetry in a-Si and a significant number of dangling bonds give rise to a reduction in the total energy of interatomic bonds required for the a-Si dissolution in comparison with crystalline Si.

In Fig. 10, the phase diagram of the Sn-Si system is plotted according to the data of work [20]. The eutectic point for the Sn:Si alloy, i.e. the minimum temperature, at which the components coexist in the liquid phase, almost coincides with the melting temperature of Sn (232 °C). From this diagram, one can see that, as the temperature of Sn:Si solution decreases to the eutectic point, the solubility of Si diminishes to very low values. In other words, for the Si crystallization to start at temperatures of 300–400 °C, even an insignificant dissolution of amorphous Si is enough. The smallest violations of the "temperature–concentration" equilibrium in the eutectic layer at the Sn–Si interface stimulate either the clustering of dissolved Si atoms into nanocrystals (if the temperature decreases or the oversaturation with respect to Si takes place) or the additional dissolution of a-Si (if the temperature or the tin concentration in the solution increases). Crystallization and dissolution change the temperature of eutectics in the direction opposite to that, which caused them, i.e. they return the system to the equilibrium. This factor governs the recurrence

of the processes of a-Si dissolution and nc-Si formation in the eutectic layer. Therefore, the system "a-Si–Sn" can be described with the use of the adiabatic approximation, in which there is no heat exchange with the environment. In the framework of this approximation, the layer of Sn–Si eutectics together with nonequilibrium flows of silicon and tin atoms from the adjacent regions acts as a self-oscillating system until a complete exhaustion of either component. As a result, Si transforms from the amorphous state into the crystalline one. A driving force of those processes is not only the difference between the internal energies of the crystalline and amorphous Si states, but also the difference between the Gibbs potentials of a-Si and nc-Si dissolutions in liquid Sn. The thermodynamics of the described mechanism deserves a separate and more detailed analysis.

An additional argument in favor of the considered mechanism is the fact that the silicon recrystallization in the tin melt is applied to purify Si from impurities [31, 32]. For this purpose, high temperatures are used, at which the solubility of Si in Sn and the dominant size of Si crystals are much larger in comparison with nanocrystals formed in our specimens. For example, in work [32], metallurgical silicon was dissolved in the Sn melt at 1200 °C (the Si solubility is approximately 15 at.%). Then the alloy temperature was lowered down to 700 °C in order to create a solution oversaturated with silicon (the Si solubility is approximately 1 at.%). As a result of the solution decay at 700 °C, there appeared polycrystalline Si flakes composed of crystals 100–200 μm in dimensions. According to the data of work [21], the maximum size of Si crystallites in liquid Sn at 300 °C was 5 nm. Nanocrystals on just this scale were observed in our experiments: in vicinities of Sn microdroplets in the Si:Sn film alloy [25], and in a vicinity of a Sn macrodroplet in this work. Even the low solubility of Si in Sn at 300 °C turns out enough for the formation of an appreciable number of such nanocrystals in Raman spectra. When silicon is deposited from the gas phase on the surface of liquid tin, the eutectic layer emerges, and the subsequent nanocrystals are formed more rapidly than if amorphous Si is dissolved. It is so because, in this case, there are no energy losses spent to break interatomic bonds of a-Si for its dissolution: free Si atoms in vapor transit immediately into liquid Sn. This mechanism explains the high formation rate of Si nanocrystals in the course of Si:Sn

alloy film deposition [23–25] and when the second Si layer was deposited on the Sn layer in this work.

5. Conclusions

The results obtained in this work confirm the model proposed by us in work [25] for the description of the mechanism of amorphous Si crystallization induced by the doping with tin. The tin-doping effect consists in 1) the emergence of microscopic droplets of metallic Sn in the bulk of amorphous Si, 2) the dissolution of amorphous silicon by liquid tin at temperatures above the Sn melting point and the formation of a Si-Sn eutectic layer, and 3) the cyclic processes of Si solution decay and recreation in Sn in the eutectic layer, which result in the dissolution of amorphous Si and the formation of nanocrystalline Si. Evidently, processes 2 and 3 compose a general mechanism of tin-induced silicon transformation from the amorphous into the crystalline state. This mechanism does not depend on the shape and the size of the interface between a-Si and liquid Sn metal; it can be either a macroscopic sandwich of Si and Sn films [3, 22], or microscopic Sn inclusions in Si films [25], or silicon balls with a tin core, as in this work. With certain specifications, the mechanism is also applicable to the description of the Si crystallization induced by other metals, which can form eutectic solutions with silicon.

The application of the considered mechanism of Si crystallization allows one, in principle, to smoothly control the number and the size of crystallites in the range of several nanometers. This possibility can serve as a ground for the development of new technologies aimed at manufacturing the cheap solar cells on the basis of nanosilicon films.

1. M.A. Green, K. Emery, Y. Hishikawa, and W. Warta, Prog. Photovolt. Res. Appl. **19**, 84 (2011).
2. D.L. Staebler and C.R. Wronski, Appl. Phys. Lett. **31**, 292 (1977).
3. M. Jeon, C. Jeong, and K. Kamisako, Mater. Sci. Technol. **26**, 875 (2010).
4. O. Nast and A.J. Hartmann, J. Appl. Phys. **88**, 716 (2000).
5. A. Chandra and B.M. Clemens, J. Appl. Phys. **96**, 6776 (2004).
6. F. Lin and M.K. Hatalis, MRS Proc. **279**, 553 (1992).
7. V.B. Neimash, A. Kraitchinskii, M. Kras'ko, O. Puzenko, C. Claeys, E. Simoen, B. Svensson, and A. Kuznetsov, J. Electrochem. Soc. **147**, 2727 (2000).
8. V.B. Neimash, A. Kraitchinskii, M. Kras'ko *et al.,* Ukr. J. Phys. **45**, 342 (2000).

9. C. Claeys, E. Simoen, V. Neimash, A. Kraitchinskii, M. Kras'ko, O. Puzenko, A. Blondeel, and P. Clauws, J. Electrochem. Soc. **148**, G738 (2001).

10. E. Simoen, C. Claeys, V.B. Neimash, A. Kraitchinskii, N. Krasko, O. Puzenko, A. Blondeel, and P. Clauws, Appl. Phys. Lett. **76**, 2838 (2000).

11. E. Simoen, C. Claeys, A.M. Kraitchinskii, M.M. Kras'ko, V.B. Neimash, and L.I. Shpinar, Solid State Phenom. **82**, 425 (2002).

12. M.L. David, E. Simoen, C. Claeys, V. Neimash, M. Kras'-ko, A. Kraitchinskii, V. Voytovych, A. Kabaldin, and J.F. Barbot, J. Phys. Condens. Matter **17**, S2255 (2005).

13. D. Girginoudi, N. Georgoulas, and F.J. Thanailakis, J. Appl. Phys. **66**, 354 (1989).

14. A. Mohamedi, M.L. Thye, M. Vergnat, G. Marchal, and M. Piecuch, Phys. Rev. B **39**, 3711 (1989).

15. G.N. Parsons, J.W. Cook, G. Lucovsky, S.Y. Lin, and M.J. Mantini, J. Vac. Sci. Technol. A **4**, 470 (1986).

16. R. Ragan, K.S. Min, and H.A. Atwater, Mater. Sci. Eng. B **87**, 204 (2001).

17. K.A. Johnson and N.W. Ashcroft, Phys. Rev. B **54**, 14480 (1996).

18. M. Vergnat, M. Piecuch, G. Marchal, and M. Gerl, Phil. Mag. B **51**, 327 (1985).

19. S.Yu. Shiryaev, J.L. Hansen, P. Kringhyj, and A.N. Larsen, Appl. Phys. Lett. **67**, 2287 (1995).

20. R.W. Olesinski and G.J. Abbaschian, Bull. Alloy Phase Diag. **5**, 273 (1984).

21. A. Mohiddon and G. Krishna, *Crystallization – Science and Technology*, edited by M.R.B. Andreeta (InTech, 2012), p. 461.

22. A. Mohiddon and G. Krishna, J. Mater. Sci. **47**, 6972 (2012).

23. V.V. Voitovych, V.B. Neimash, N.N. Krasko, A.G. Kolosiuk, V.Yu. Povarchuk, R.M. Rudenko, V.A. Makara, R.V. Petrunya, V.O. Yukhimchuk, and V.V. Strelchuk, Semiconductors **45**, 1281 (2011).

24. V.B. Neimash, V.M. Poroshin, O.M. Kabaldin, P.E. Shepelyaviy, V.O. Yukhymchuk, V.A. Makara, and S.U. Larkin, Ukr. J. Phys. **58**, 865 (2013).

25. V. Neimash, V. Poroshin, P. Shepeliavyi, V. Yukhymchuk, V. Melnyk, A. Kuzmich, V. Makara, and A. Goushcha, J. Appl. Phys. **113**, 213104 (2013).

26. H. Richter, Z.P. Wang, and L. Ley, Solid State Commun. **39**, 625 (1981).

27. H. Cambell and P.M. Fauchet, Solid State Commun. **58**, 739 (1986).

28. A. Hiraki, Surf. Sci. Rep. **3**, 357 (1984).

29. M. Hillert, Acta Metallur. **9**, 525 (1961).

30. A.G. Milnes, *Deep Impurities in Semiconductors* (Wiley, New York, 1973).

31. G.F. Wakefield and H.S. Nagaraja Setty, *Patent US 3933981 A* (20.01.1976).

32. I.E. Maronchuk, T.F. Kulyutkina, and I.I. Maronchuk, *Patent UA 84653* (16.02.2010).

В.Б. Неймаш, О.О. Гуща,
П.Є. Шепелявий, В.О. Юхимчук, В.А. Данько,
В.В. Мельник, А.Г. Кузьмич

МЕХАНІЗМ ІНДУКОВАНОЇ ОЛОВОМ
КРИСТАЛІЗАЦІЇ АМОРФНОГО КРЕМНІЮ

Р е з ю м е

Методами оже-спектроскопії, електронної мікроскопії та комбінаційного розсіювання світла експериментально досліджено формування нанокристалів Si в плівкових структурах аморфний Si–металеве Sn. Результати проаналізовані в сукупності з недавніми даними про кристалізацію аморфного Si, легованого оловом. Запропоновано механізм трансформації кремнію із аморфного у нанокристалічний стан у евтектичному шарі на інтерфейсі Si–Sn. Суть механізму полягає у циклічному повторенні процесів утворення і розпаду розчину Si у Sn. Розглянуто прикладний аспект використання цього механізму у виробництві плівкового нанокремнію для сонячних елементів.